OPEN ACCESS



TOI-4201: An Early M Dwarf Hosting a Massive Transiting Jupiter Stretching Theories of Core Accretion*

```
Megan Delamer<sup>1,2</sup>, Shubham Kanodia<sup>3</sup>, Caleb I. Cañas<sup>4,22</sup>, Simon Müller<sup>5</sup>, Ravit Helled<sup>5</sup>, Andrea S. J. Lin<sup>1,2</sup>, Jessica E. Libby-Roberts<sup>1,2</sup>, Arvind F. Gupta<sup>1,2</sup>, Suvrath Mahadevan<sup>1,2</sup>, Johanna Teske<sup>3</sup>, R. Paul Butler<sup>3</sup>,
   Samuel W. Yee<sup>6</sup>, Jeffrey D. Crane<sup>7</sup>, Stephen Shectman<sup>7</sup>, David Osip<sup>8</sup>, Yuri Beletsky<sup>8</sup>, Andrew Monson<sup>9</sup>, Leslie Hebb<sup>10,11</sup>, Luke C. Powers<sup>1,2</sup>, John P. Wisniewski<sup>12</sup>, Jaime A. Alvarado-Montes<sup>13,14</sup>, Chad F. Bender<sup>9</sup>,
         Jiayin Dong 15,23 , Te Han 16 , Joe P. Ninan 17 , Paul Robertson 16 , Arpita Roy 18,19 , Christian Schwab 13 ,
                                                    Guðmundur Stefánsson<sup>20,24</sup>, and Jason T. Wright<sup>1,2,21</sup>
Department of Astronomy & Astrophysics, 525 Davey Laboratory, The Pennsylvania State University, University Park, PA 16802, USA; mmd6393@psu.edu
              Center for Exoplanets and Habitable Worlds, 525 Davey Laboratory, The Pennsylvania State University, University Park, PA 16802, USA
                      Earth and Planets Laboratory, Carnegie Institution for Science, 5241 Broad Branch Road NW, Washington, DC 20015, USA

NASA Goddard Space Flight Center, 8800 Greenbelt Road, Greenbelt, MD 20771, USA
                     <sup>5</sup> Center for Theoretical Astrophysics & Cosmology, University of Zurich, Winterthurerstr. 190, CH-8057 Zurich, Switzerland <sup>6</sup> Department of Astrophysical Sciences, Princeton University, 4 Ivy Lane, Princeton, NJ 08544, USA
                            <sup>7</sup> The Observatories of the Carnegie Institution for Science, 813 Santa Barbara Street, Pasadena, CA 91101, USA
                                 Las Campanas Observatory, Carnegie Institution for Science, Colina el Pino, Casilla 601 La Serena, Chile
                                   Steward Observatory, The University of Arizona, 933 North Cherry Avenue, Tucson, AZ 85721, USA
                                Physics Department, Hobart and William Smith Colleges, 300 Pulteney Street, Geneva, NY 14456, USA
                                            Department of Astronomy, Cornell University, 245 East Avenue, Ithaca, NY 14850, USA
                                                NASA Headquarters, 300 Hidden Figures Way SW, Washington, DC 20546, USA
                     <sup>13</sup> School of Mathematical and Physical Sciences, Macquarie University, Balaclava Road, North Ryde, NSW 2109, Australia
The Macquarie University Astrophysics and Space Technologies Research Centre, Macquarie University, Balaclava Road, North Ryde, NSW 2109, Australia

15 Center for Computational Astrophysics, Flatiron Institute, New York, NY, USA
                                   Department of Physics & Astronomy, The University of California, Irvine, Irvine, CA 92697, USA
           <sup>17</sup> Department of Astronomy and Astrophysics, Tata Institute of Fundamental Research, Homi Bhabha Road, Colaba, Mumbai 400005, India
<sup>18</sup> Space Telescope Science Institute, 3700 San Martin Drive, Baltimore, MD 21218, USA
                     <sup>19</sup> Department of Physics and Astronomy, Johns Hopkins University, 3400 North Charles Street, Baltimore, MD 21218, USA
                                     Department of Astrophysical Sciences, Princeton University, 4 Ivy Lane, Princeton, NJ 08540, USA
          <sup>21</sup> Penn State Extraterrestrial Intelligence Center, 525 Davey Laboratory, The Pennsylvania State University, University Park, PA, 16802, USA
                               Received 2023 July 13; revised 2023 December 7; accepted 2023 December 9; published 2024 February 13
```

Abstract

We confirm TOI-4201 b as a transiting Jovian-mass planet orbiting an early M dwarf discovered by the Transiting Exoplanet Survey Satellite. Using ground-based photometry and precise radial velocities from NEID and the Planet Finder Spectrograph, we measure a planet mass of $2.59^{+0.07}_{-0.06}~M_{\rm J}$, making this one of the most massive planets transiting an M dwarf. The planet is $\sim 0.4\%$ of the mass of its $0.63~M_{\odot}$ host and may have a heavy-element mass comparable to the total dust mass contained in a typical class II disk. TOI-4201 b stretches our understanding of core accretion during the protoplanetary phase and the disk mass budget, necessitating giant planet formation to take place either much earlier in the disk lifetime or perhaps through alternative mechanisms like gravitational instability.

Unified Astronomy Thesaurus concepts: Exoplanet detection methods (489); Exoplanet astronomy (486); Exoplanet formation (492); Exoplanets (498); Radial velocity (1332); Transit photometry (1709); Extrasolar gaseous giant planets (509)

Supporting material: machine-readable table

1. Introduction

The Transiting Exoplanet Survey Satellite (TESS; Ricker et al. 2014) observes millions of stars across the entire sky searching for transiting candidates. It has been instrumental in

Original content from this work may be used under the terms of the Creative Commons Attribution 4.0 licence. Any further distribution of this work must maintain attribution to the author(s) and the title of the work, journal citation and DOI.

finding planets around M dwarf stars, the most common type of star in the Galaxy. Among the confirmed TESS candidate planets orbiting M dwarfs are ~ 15 giant planets in short-period orbits (e.g., Gan et al. 2022; Hobson et al. 2023; Kagetani et al. 2023; Kanodia et al. 2023), which seem to challenge current theories of planet formation through core accretion (Laughlin et al. 2004; Ida & Lin 2005).

Under the core accretion model, the formation of giant exoplanets around M dwarf stars (GEMS) is difficult for two main reasons. First, we expect disk mass, particularly the solid surface density, to scale with host star mass (Andrews et al. 2013; Pascucci et al. 2016). Under typical opacity assumptions, runaway gas accretion can only be triggered after a core of $\sim 10\,M_\oplus$ is formed (Stevenson 1982; Pollack et al. 1996). Since $10\,M_\oplus$ is a large percentage of the solid

^{*} This paper includes data gathered with the 6.5 m Magellan Telescopes located at Las Campanas Observatory, Chile.

NASA Postdoctoral Fellow.

²³ Flatiron Research Fellow.

²⁴ NASA Sagan Fellow.

mass typically available in a disk around an M dwarf (Ansdell et al. 2016; Tazzari et al. 2021; Manara et al. 2023), forming this core would be a challenge. Second, due to their lower masses, the Keplerian orbital timescales are much longer for M dwarfs compared to solar-type stars, which, coupled with their lower disk surface densities, should make it harder to form a massive enough core in time to initiate runaway gaseous accretion before the disk dissipates (Laughlin et al. 2004).

Previous work on FGK stars has found that the frequency of giant planets increases with stellar mass (Johnson et al. 2010; Fulton et al. 2021), supporting the general conclusions of the core accretion model. However, results from microlensing surveys indicate that giant planets could form more frequently around M dwarfs than what has been seen in Doppler surveys, but these microlensing surveys probe a different area of parameter space and still indicate a decreased occurrence rate relative to FGK stars (Gould et al. 2010; Clanton & Gaudi 2014). The discovery and characterization of these GEMS is already challenging our understanding of giant planet formation, and despite their enhanced detection probabilities for transit and radial velocity (RV) observations (large planet to stellar mass and radius ratios), they remain rare. While it is currently difficult to perform accurate sample-level comparisons on the existing population (<15), efforts are underway to significantly increase this sample size and enable such analysis in the future.

In this letter, we present the confirmation of a massive super-Jupiter around the early M dwarf TOI-4201. While previous gas giants have been difficult to explain from a mass budget perspective (Hobson et al. 2023; Kanodia et al. 2023), one proposed explanation is that planet formation begins early on in the disk lifetime (<1 Myr), when the disks are much more massive. The discovery of a super-Jupiter around an early M dwarf with a planet-to-host mass ratio of \sim 0.4% stretches this even further.

To characterize TOI-4201 and confirm the TESS signal as a planet, we use precision RVs from NEID and the Planet Finder Spectrograph (PFS), high-contrast speckle imaging from the WIYN NN-Explore Exoplanet Stellar Speckle Imager (NESSI), and ground-based photometry from the Three-hundred Milli-Meter Telescope (TMMT) and Las Campanas Remote Observatory (LCRO), as well as archival photometry from the Las Cumbres Observatory global telescope network (LCOGT). We detail these observations in Section 2 and describe the stellar characterization in Section 3. Section 4 covers the data analysis, including details of the joint modeling of RVs and photometry. In Section 5, we compare TOI-4201 b with other giant planets around M dwarfs and consider potential formation scenarios. We summarize our findings in Section 6.

2. Observations

2.1. TESS

TOI-4201 (TIC 95057860, Gaia DR3 2997312063605005056) was identified as hosting a transiting object of interest in the TESS Sector 6 long-cadence (1800 s) light curve spanning 2018 December 11 to 2019 January 7 by the Quick Look Pipeline (Huang et al. 2020) during the Faint Star Search (Kunimoto et al. 2022). It was reobserved by TESS during Sector 33 from 2020 December 17 to 2021 January 13 with 600 s cadence. We extract

a light curve for each sector by performing aperture photometry with eleanor (Feinstein et al. 2019) using the CORR_FLUX values, in which eleanor uses linear regression with pixel position, measured background, and time to remove signals correlated with these parameters. We show the TESS photometry in Figure 1.

2.2. Ground-based Photometric Follow-up

2.2.1. 3.5 m ARC Telescope

We observed a transit of TOI-4201 b on the night of 2022 February 9 with the Astrophysical Research Consortium (ARC) Telescope Imaging Camera (ARCTIC; Huehnerhoff et al. 2016) on the ARC 3.5 m telescope at Apache Point Observatory. We conducted this observation with an engineered diffuser, which allows for near scintillation-limited light curves by spreading the stellar point-spread function into a controllable top-hat profile without defocusing the telescope (Stefansson et al. 2017). The observations for the night used quad-amplifier and fast readout mode with 4×4 pixel binning and $40 \, \mathrm{s}$ exposures. We took biases and sky flats prior to beginning observations, but ARCTIC does not experience significant dark current for observations of $<60 \, \mathrm{s}$; therefore, this was not accounted for in our reduction.

We observed TOI-4201 b in Sloan Digital Sky Survey (SDSS) i' while the target set from an air mass of 1.44 to 4.47. We processed the photometry using AstroImageJ (Collins et al. 2017). We plot the final light curves in Figure 1.

2.2.2. TMMT and LCRO

We observed a transit of TOI-4201 b on the night of 2021 December 28 with the TMMT (Monson et al. 2017) at Las Campanas Observatory with 120 s exposures in Bessell *I*. Observations were taken as the target set from an air mass of 1.19 to 2.48.

We then observed a second transit on the night of 2022 January 15, with TMMT in Bessell V and the 0.6 m LCRO in SDSS i', both using 300 s exposures. The target set from an air mass of 1.04 to 1.66 over the course of the night.

We reduced the data from all three observations (bias correction, flat-fielding, cosmic-ray/bad-pixel removal, etc.) following the procedure outlined in Monson et al. (2017). Then, we performed differential aperture photometry on all images using a python script based on Monson et al. (2017). Final light curves are plotted in Figure 1.

2.2.3. 1.0 m LCOGT Archival Data

We also retrieve a full transit for TOI-4201 b from the LCOGT (Brown et al. 2013) public data archive. This transit was observed in both SDSS g' and i' on the night of 2021 October 3 (proposal ID: KEY2020B-005; PI: A. Shporer) from the Sinistro imaging camera on the 1 m LCOGT Dome B telescope at Cerro Tololo Inter-American Observatory. These observations were taken mildly defocused (FWHM \sim 2."5) at exposure times of 300 s in g' and 180 s in i', with the target rising from an air mass of \sim 2.3 to 1.06 over the course of the night. Mildly defocusing the telescope reduces the effects of variations in individual pixels by spreading the light from the source over many pixels (Southworth et al. 2009; Mann et al. 2011). The raw data were automatically

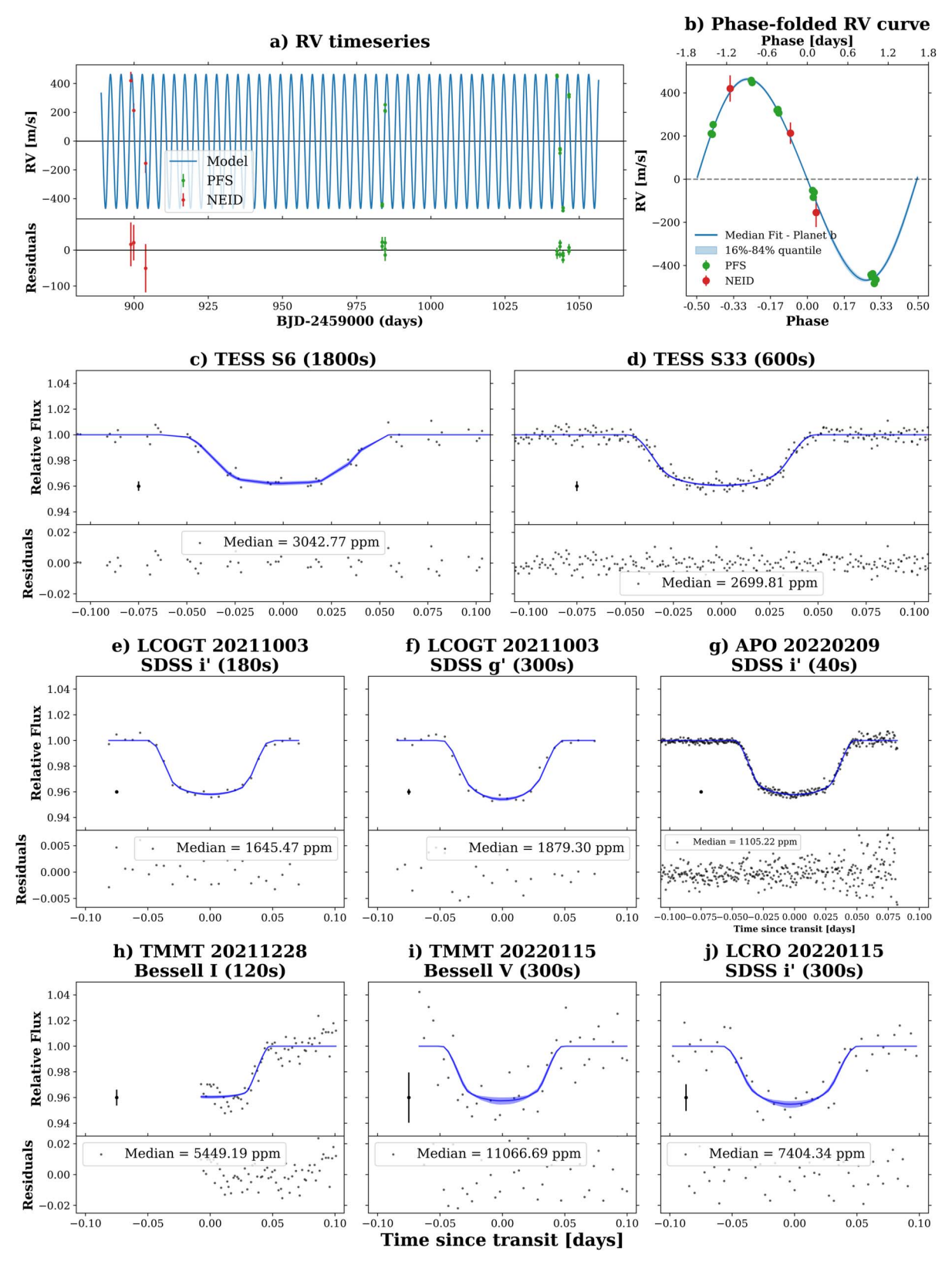


Figure 1. Figure including all photometric and RV observations used in the analysis of TOI-4201 b. (a) Time series of RV observations of TOI-4201 b with NEID (red) and PFS (green). The best-fitting model from the joint fit is plotted in blue, and residuals after subtracting the fit are included below. (b) NEID and PFS observations phase-folded on the best-fit orbital period from the joint fit, with the model in blue and 16%-84% confidence levels in light blue. (c)-(i) Photometric observations of TOI-4201 b; in all plots, the detrended data are in gray, and the model and 16%-18% confidence levels are in blue. In each figure, the point at x = -0.075 represents the median uncertainty in the photometric data.

processed by the BANZAI pipeline (McCully et al. 2018). We then perform aperture photometry on the processed images using AstroImageJ (Collins et al. 2017). We see a

strong slope in both the g' and i' light curves, so we detrend both data sets in time prior to our analysis. These transits are shown in panels (e) and (f) of Figure 1.

Table 1 RVs for TOI-4201

BJD _{TDB}	RV	σ	Instrument
(days)	$(m s^{-1})$	$(m s^{-1})$	morament
2459898.89219	124.5	61.1	NEID
2459899.87168	-82.3	49.4	NEID
2459903.87132	-450.0	67.3	NEID
2459983.56562	-390.7	13.9	PFS
2459983.57882	-400.1	11.5	PFS
2459983.59321	-386.2	14.1	PFS
2459984.55132	263.3	15.5	PFS
2459984.56623	259.4	16.6	PFS
2459984.58013	304.9	16.3	PFS
2460042.51200	509.6	10.2	PFS
2460042.52631	499.5	12.8	PFS
2460043.50692	0.0	9.7	PFS
2460043.52043	-32.1	8.6	PFS
2460043.53418	-9.1	8.2	PFS
2460044.51157	-431.8	8.9	PFS
2460044.52556	-410.4	9.5	PFS
2460044.53970	-413.8	10.6	PFS
2460046.51302	371.3	10.0	PFS
2460046.52716	374.8	9.8	PFS
2460046.54106	358.9	9.6	PFS

(This table is available in machine-readable form.)

2.3. High-contrast Imaging

2.3.1. NESSI

We observed TOI-4201 on the night of 2022 April 18 with NESSI (Scott et al. 2018) on the WIYN²⁵ 3.5 m telescope at Kitt Peak National Observatory to rule out stellar companions. We took diffraction-limited exposures using the red camera and the Sloan z' filter at a 40 ms cadence for 9 minutes and reconstructed the speckle image following the methods described by Howell et al. (2011). We compute 5σ contrast limits as a function of separation, $\Delta\theta$, from the primary source and find no evidence for nearby or background sources with $\Delta z' < 3.5$ at $\Delta \theta = 0.75$ and $\Delta z' < 3.9$ at $\Delta \theta = 1.72$.

2.4. RV Follow-up

2.4.1. NEID

We observed TOI-4201 using NEID, a fiber-fed, environmentally stabilized spectrograph on the WIYN 3.5 m telescope (Halverson et al. 2016; Schwab et al. 2016; Robertson et al. 2019) for three epochs between 2022 November 15 and 2022 November 20. NEID covers the wavelength range 380–930 nm with a spectral resolution of $R \sim 110,000$. Each visit consisted of a single 30 minute exposure. We use the standard NEID data reduction pipeline followed by the SERVAL algorithm developed by Zechmeister et al. (2018) and adapted for NEID by Stefànsson et al. (2022). At 850 nm, the signal-to-noise ratio for each of the three RV points is 6.0, 7.6, and 5.5; we attribute the high jitter seen in the fit to the low signal-to-noise ratio. The

final NEID RVs are included in Table 1 and as a machinereadable table with the manuscript.

2.4.2. PFS

We observed TOI-4201 with the PFS (Crane et al. 2006, 2008, 2010) on the 6.5 m Magellan II (Clay) telescope at Las Campanas Observatory. Between 2022 November 8 and 2023 April 12, we obtained six visits, each consisting of three exposures of $1200 \,\mathrm{s}^{26}$ in 3×3 CCD binning mode with a 0."3 slit. These data were taken with the iodine gas absorption cell in the light path, which imprints a dense forest of molecular lines (Hatzes 2019) between 5000 and 6200 Å. We also obtained one template spectrum without the iodine cell consisting of six exposures of 1200 s. The RVs were derived following the methodology of Butler et al. (1996). As noted by Hartman et al. (2015) and Bakos et al. (2020), due to the faintness of the target and the optical region for the iodine region, the formal errors on the PFS RVs are likely underestimated. The final PFS RVs are included in Table 1 and as a machine-readable table with the manuscript.

3. Stellar Parameters

The stellar parameters presented in Table 2 are derived using the available broadband photometry and Gaia astrometry. The stellar metallicity is estimated as $[Fe/H] = 0.30 \pm 0.15$ using Wide-field Infrared Survey Explorer (WISE) and Gaia colors² (Equation (4) from Duque-Arribas et al. 2023). This photometric relationship was determined by Duque-Arribas et al. (2023) to be the most accurate photometric calibration when compared to a well-characterized (i) spectroscopic sample of M dwarfs (Birky et al. 2020) and (ii) M dwarfs in binary systems (Montes et al. 2018). The stellar radius is calculated as $R_{\star} = 0.62 \pm 0.02 \ R_{\odot}$ using Equation (5) from Mann et al. (2015), an empirical relationship that relies on the stellar metallicity derived above and the absolute K-band magnitude. This radius value was then used to empirically determine a mass of $M_{\star} = 0.63 \pm 0.02$ M_{\odot} with Equation (6) from Schweitzer et al. (2019), which also agrees with the stellar mass estimate from Mann et al. (2019). The stellar effective temperature is derived as 3920 ± 50 K with the empirical calibration from Equation (7) in Rabus et al. (2019), which was derived using interferometric observations of well-characterized M dwarfs. The adopted stellar parameters are consistent at the 1σ level with the (i) Bayesian stellar parameters $[\text{Fe/H}] = 0.300^{+0.002}_{-0.388}, M_{\star} = 0.65^{+0.002}_{-0.050} M_{\odot}, T_{\text{eff}} = 3955^{+20}_{-49} \text{ K})$ derived using the StarHorse code and a combination of multiwavelength photometry and Gaia parallaxes (Anders et al. 2022) and (ii) stellar parameters derived from a fit to the spectral energy distribution using EXOFASTv2 (using the broadband photometry in Table 2, $M_{\star} = 0.62 \pm 0.03 M_{\odot}$, $R_{\star} = 0.60 \pm$ $0.02 R_{\odot}$, $T_{\rm eff} = 3890 \pm 70$ K; Eastman et al. 2019).

3.1. Galactic Kinematics

We calculate the UVW velocities in the barycentric frame and relative to the local standard of rest from Schönrich et al. (2010) using GALPY (Bovy 2015).²⁸ These velocities are

²⁵ The WIYN Observatory is a joint facility of the NSF's National Optical-Infrared Astronomy Research Laboratory, Indiana University, the University of Wisconsin-Madison, Pennsylvania State University, the University of Missouri, the University of California-Irvine, and Purdue University.

Barring the visit on 2023 April 8 (BJD 2460042.512), which had to be cut short after two exposures due to adverse weather.

27 See https://chrduque.shinyapps.io/metamorphosis/.

Following the convention of U toward the Galactic center, V toward the direction of Galactic spin, and W toward the north Galactic pole.

reported in Table 2 and used to classify TOI-4201 as a thin disk star using the criteria from Bensby et al. (2014). TOI-4201 is also determined to be a field star (>99% change of membership) using the BANYAN Σ tool (Gagné et al. 2018).

4. Joint Fitting of Photometry and RVs

We performed joint fitting of the RV time series and the photometric curves using exoplanet (Foreman-Mackey et al. 2021b), a software package that utilizes PyMC3, a Hamiltonian Monte Carlo (HMC) posterior sampling algorithm (Salvatier et al. 2016). HMC is a Markov Chain Monte Carlo method that uses first-order gradients to avoid random walk behavior that is further improved by the implementation of the No U-Turn Sampler, which reduces sensitivity to user-specified parameters (Hoffman & Gelman 2014). We use a Keplerian orbit to model the RVs, leaving the eccentricity as a free parameter because the phase coverage on the RV data is complete enough to offer a constraint. A linear trend and RV offsets for each instrument were fit to the data to account for long-term changes from both astrophysical and instrumental causes.

We modeled the transits using starry (Luger et al. 2019; Agol et al. 2020), which uses the analytic formulae derived in Mandel & Agol (2002) to compute the light curves based on model stellar atmospheres and relies on separate quadratic limb-darkening parameters for each filter. During the joint fit with all RV and photometric instruments, we fit each phased transit with separate limb-darkening coefficients. A jitter term was fit for each data set as a white-noise model that was then added in quadrature to the uncertainty of the data sets. For instruments that exhibited a visible trend, we included a linear term in the fit. We used celerite2 (Foreman-Mackey et al. 2017; Foreman-Mackey 2018) to include a Gaussian process kernel in the likelihood function of the TESS data to model the quasiperiodic signal.

While the radius derived from photometric data sets can vary across wavelengths due to differing opacities of atmospheric molecules, our observations are not precise enough to probe this difference. To check for chromaticity across the groundbased transits, we included a dilution term for all but one and confirmed all were consistent with a value of 1. This value indicates that none of the ground-based photometry suffered from contamination due to background stars. We therefore adopt a value of 1 for the dilution term for all ground-based transits. A dilution term, D_{TESS} , is included for each of the two TESS transits, as the larger pixel scale can lead to contamination from background stars that alter the transit signal. We assume the ground-based transits do not experience flux contamination due to their higher spatial resolution and use them to correct the TESS photometry. We fit a separate term for each sector due to variations in the placement of the target and background stars on the detector pixels.

The joint fit included 65 free parameters, and convergence was mathematically determined based on the Gelman–Rubin statistic. The final derived planet parameters from the joint fit are included in Table 3, and the phased transits and RVs are shown in Figure 1. While we estimate a nonzero eccentricity, we note that this is dominated by the PFS observations as evinced by the low RV jitter compared to NEID. Previous work on HATS-6 b also derived a nonzero eccentricity using PFS

 Table 2

 Summary of Stellar Parameters for TOI-4201

Main Identifie TOI TIC	TESS object of	4201	
	•	4201	
TIC	:	7201	TESS mission
TIC	interest		
	TESS Input	95057860	Stassun
	Catalogue		
2MASS	•••	J06015391-1327410	2MASS
Gaia DR3		2997312063605005056	Gaia DR3
•	ordinates and Proper M		G : DD2
$\alpha_{\rm J2000}$	R.A.	90.475 ± 0.014	Gaia DR3
$\delta_{ m J2000}$	decl.	-13.461 ± 0.015	Gaia DR3
μ_{α}	Proper motion	11.731 ± 0.017	Gaia DR3
	$(R.A., mas yr^{-1})$	6050 1 0010	G : DD2
μ_{δ}	Proper motion	6.053 ± 0.018	Gaia DR3
	(decl., mas yr ⁻¹)		
$\overline{\omega}$	Parallax in mas	5.291 ± 0.019	Gaia DR3
d	Distance in pc	$187.5^{+0.6}_{-0.7}$	Bailer-Jones
	ear-infrared Magnitude		
	Johnson B mag	16.69 ± 0.15	APASS
	Johnson V mag	15.28 ± 0.04	APASS
g'	Sloan g' mag	16.00 ± 0.05	APASS
r'	Sloan r' mag	14.67 ± 0.08	APASS
i'	Sloan i' mag	13.91 ± 0.11	APASS
J	J mag	12.258 ± 0.021	2MASS
H	H mag	11.564 ± 0.024	2MASS
K_s	K_s mag	11.368 ± 0.025	2MASS
W1	WISE1 mag	11.272 ± 0.024	WISE
W2	WISE2 mag	11.301 ± 0.021	WISE
W3	WISE3 mag	11.283 ± 0.155	WISE
Photometric R	telations		
$T_{ m eff}$	Effective temper-	3920 ± 50	This work
	ature in K		
[Fe/H]	Metallicity in dex	0.30 ± 0.15	This work
M_{\star}	Mass in M_{\odot}	0.63 ± 0.02	This work
R_{\star}	Radius in R_{\odot}	0.62 ± 0.02	This work
Other Stellar			
	Surface gravity in cgs units	4.65 ± 0.03	This work
L_{\star}	Luminosity in L_{\odot}	0.081 ± 0.007	This work
ρ_{\star}	Density in g cm ⁻³	3.7 ± 0.4	This work
ΔRV	"Absolute" RV in km s ⁻¹	42.07 ± 0.14	This work
U, V, W	Galactic velocities	-34.0 ± 0.1 ,	This work
	in ${\rm km}~{\rm s}^{-1}$	-27.46 ± 0.09 ,	
		-0.97 ± 0.06	
U, V, W^{a}	Galactic velocities	-22.9 ± 0.8 ,	This work

Notes.

References. Stassun (Stassun et al. 2018), 2MASS (Cutri et al. 2003), Gaia DR3 (Gaia Collaboration et al. 2023), Bailer-Jones (Bailer-Jones et al. 2021), APASS (Henden et al. 2018), WISE (Wright et al. 2010).

that was inconsistent with stellar parameters, and it was suggested that there may be an underestimation of the formal RV errors when it comes to faint targets (Hartman et al. 2015). While we formally adopt the eccentric fit here in the interest of completeness, we caution against overinterpretation of this tentative eccentricity detection.

^a The barycentric *UVW* velocities are converted into local standard of rest (LSR) velocities using the constants from Schönrich et al. (2010).

 Table 3

 Planetary Parameters for the TOI-4201 System

Parameter	Units	Value ^a
Orbital Parameters		
Orbital period	P (days)	3.5819232 ± 0.0000024
Eccentricity	e	0.062 ± 0.019
Argument of periastron	ω (rad)	$-1.65^{+0.14}_{-0.23}$
Semiamplitude velocity	$K \text{ (m s}^{-1})$	$466.6^{+5.5}_{-5.8}$
Systemic velocity ^b	$\gamma_{ m NEID}~({ m m~s}^{-1})$	-296^{+57}_{-64}
	$\gamma_{\rm PFS}~({ m m~s}^{-1})$	$51.6^{+4.8}_{-4.7}$
RV trend	$dv/dt \text{ (m s}^{-1} \text{ yr}^{-1})$	-0.8 ± 4.9
RV jitter	$\sigma_{\rm NEID}~({\rm m~s}^{-1})$	67^{+150}_{-50}
	$\sigma_{\rm PFS}~({\rm m~s^{-1}})$	$13.2^{+5.7}_{-4.5}$
Transit Parameters		
Transit midpoint	T_C (BJD _{TDB})	$2459205.25532^{+0.00027}_{-0.00026}$
Scaled radius	R_p/R_*	$0.1930^{+0.0018}_{-0.0020}$
Scaled semimajor axis	a/R_*	$14.05^{+0.32}_{-0.31}$
Orbital inclination	i (deg)	$88.24^{+0.14}_{-0.13}$
Transit duration	T_{14} (days)	$0.0894^{+0.0019}_{-0.0018}$
Photometric jitter ^c	$\sigma_{\rm TESS~S6}$ (ppm)	2870^{+180}_{-170}
	$\sigma_{\rm TESS~S33}$ (ppm)	1420^{+140}_{-150}
	σ _{LCO 20211003 i} (ppm)	1950^{+490}_{-400}
	$\sigma_{\rm LCO~20211003~g}~({\rm ppm})$	2380^{+840}_{-930}
	$\sigma_{\text{TMMT }20211228}$ (ppm)	2000^{+2400}_{-2100}
	$\sigma_{\rm TMMT\ 20220115}\ ({\rm ppm})$	80^{+1600}_{-70}
	$\sigma_{\rm LCRO~20220115}~({\rm ppm})$	60^{+1000}_{-60}
Dilution ^d , e	$D_{\mathrm{TESS~S6}}$	$0.937^{+0.038}_{-0.036}$
	$D_{\mathrm{TESS~S33}}$	$0.897^{+0.017}_{-0.016}$
Planetary Parameters		
Mass	$M_{\rm p}~(M_{\oplus})$	825^{+20}_{-19}
	$M_{\rm p}~(M_{\rm J})$	$2.595^{+0.063}_{-0.060}$
Radius	$R_{\rm p}~(R_{\oplus})$	12.69 ± 0.33
	$R_{\rm p} (R_{\rm J})$	1.132 ± 0.029
Density	$\rho_{\rm p}~({\rm g~cm}^{-3})$	$2.22^{+0.18}_{-0.16}$
Semimajor axis	a (au)	$0.03944^{+0.00039}_{-0.00040}$
Average incident flux ^f	$\langle F \rangle$ ($10^5 \mathrm{W} \;\mathrm{m}^{-2}$)	0.675 ± 0.048
Planetary insolation	$S(S_{\oplus})$	49.6 ± 3.5
Equilibrium temperature	$T_{\rm eq}$ (K)	739 ± 13

Notes

5. Discussion

5.1. Placing TOI-4201 b in Context

TOI-4201 b is a massive Jovian planet with a radius of $1.13 \pm 0.03~R_{\rm J}$, mass of $2.60 \pm 0.06~M_{\rm J}$, and bulk density of $2.2 \pm 0.2~{\rm g~cm^{-3}}$. Orbiting a metal-rich M dwarf host star $(M_{\star}=0.63 \pm 0.02~M_{\odot})$, it joins a small but growing number of GEMS with precise masses and radii. In Figure 2, we plot TOI-4201 b together with all known transiting giant planets $(R>4~R_{\oplus})$ around M dwarfs up to $T_{\rm eff}<4100~{\rm K}$ to account for host stars on the late K/early M border in the first panel. Subsequent panels use a cutoff of $T_{\rm eff}<4000~{\rm K}$.

Using data from the NASA Exoplanet Archive (Akeson et al. 2013; NASA Exoplanet Archive 2023), in Figure 2, we show that the closest grouping in mass-radius space to TOI-4201 b consists of HATS-76 b and HATS-77 b (Jordán et al. 2022), both of which orbit stars that are on the edge between late K and early M dwarfs. Of particular note is the similarity in radius between TOI-4201 b and HATS-77 b; despite both planets orbiting old inactive stars²⁹ and neither planet experiencing sufficient irradiation to inflate the radius (Demory & Seager 2011), both have somewhat larger radii than models would suggest (Mordasini et al. 2012). In order to characterize the interior of TOI-4201 b and quantify the degree of inflation, we use the giant planet evolution models from Müller & Helled (2021) and calculate the cooling for different possible heavy-element masses. Using the derived planetary parameters, these models suggest that the planet is inflated by a few percent beyond what would be expected for a planet with a pure H/He composition as shown in Figure 3.

Previous work has found that the assumptions underlying interior models of giant planets can cause variations in the predicted radius on the order of a few percent (for a review, see Müller & Helled 2023). The main culprits appear to be uncertainties in the H-He equations of state (Müller et al. 2020a; Howard & Guillot 2023) and the opacity (Müller et al. 2020a). The impacts of these factors on the radius are shown in Figures 4 and 5. These cooling curves include an additional giant planet evolution model (S. Müller et al. 2023, in preparation) that uses an updated equation of state that includes nonideal mixing effects (Chabrier & Debras 2021), which the authors consider to be the most reliable of the options presented in Figure 4. While earlier versions of the H/He equation of state could explain the planet's inflated radius, the additional physics being taken into account in more modern iterations decreases the likelihood that discrepancies from the equation of state alone could explain the apparent inflation. The calculations including varying grain opacity demonstrate that a significant additional opacity source would be needed to explain the inflation. While previous work suggests that the grain opacity in embedded planets is 0.1%-1% of the interstellar medium value (Podolak 2003; Movshovitz & Podolak 2008; Movshovitz et al. 2010; Mordasini et al. 2014), the details of the grain opacity for conditions relevant to TOI-4201 b are less clear. The number and size of grains present in planetary atmospheres under these conditions are highly uncertain and depend on many parameters, such as the composition and the condensation microphysics (Marley et al. 2013; Cuzzi et al. 2014).

Additionally, current evolution models of giant exoplanets assume that their interiors are fully convective. However, there is evidence that Jupiter and Saturn have regions that are not fully convective today due to composition gradients (Debras et al. 2021; Mankovich & Fuller 2021). This could suggest that giant planets do not cool solely by large-scale convection, and therefore their interiors may be hotter, leading to inflated radii of up to about 10% past 1 Gyr (Kurokawa & Inutsuka 2015). However, it is currently unclear whether these composition gradients could be sustained over a few Gyr (Müller et al. 2020b). To explain the apparent inflation of TOI-4201 b, either its cooling must be slowed by the aforementioned mechanisms,

^a The reported values refer to the 16th–50th–84th percentile of the posteriors.

b In addition to the "Absolute RV" from Table 2.

^c Jitter (per observation) added in quadrature to photometric instrument error.

^d Dilution due to presence of beek ground stors in TESS enerting not accounted

 $^{^{\}rm d}$ Dilution due to presence of background stars in TESS aperture not accounted for in the eleanor flux.

 $^{^{\}rm e}$ We use a solar flux constant = 1360.8 W $\rm m^{-2}$ to convert insolation to incident flux.

^f We assume the planet to be a blackbody with zero albedo and perfect energy redistribution to estimate the equilibrium temperature.

²⁹ While we do not have a precise age constraint on TOI-4201, the photometry and spectroscopic observations do not contain activity signatures common to young stars, suggesting an old system.

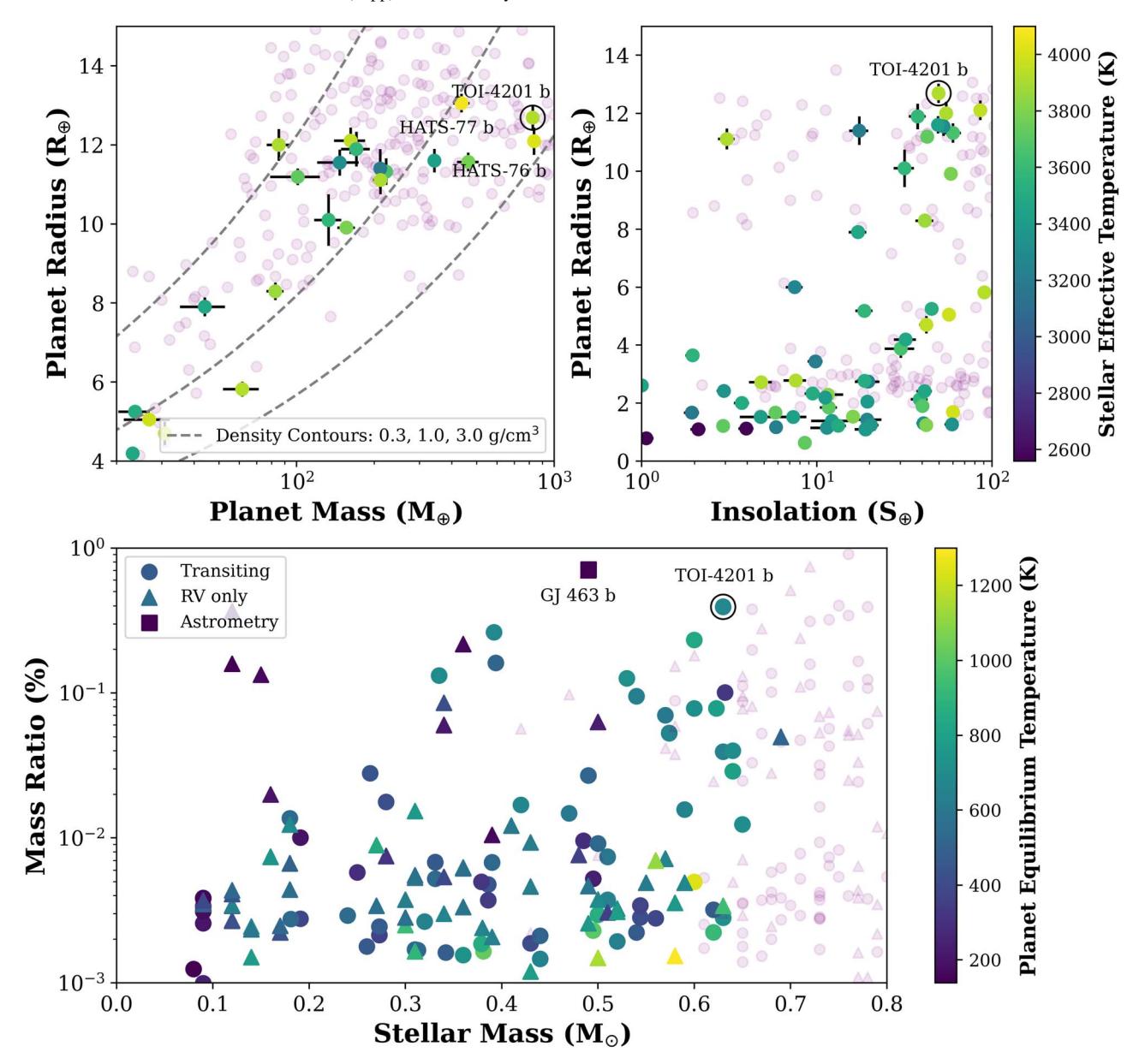


Figure 2. Upper left: we include TOI-4201 b (circled in black) on a mass-radius plane, with planets colored by host star temperature. We include planets around FGK stars in the background, and gray contours indicate bulk densities of 0.3, 1.0, and 3.0 g cm⁻³ (left to right). Upper right: TOI-4201 b in an insolation-radius plane for the same sample of planets. Lower: planet-to-star mass ratio vs. host star mass, colored by equilibrium temperature. Planets with a true mass measurement from transit observations are represented by circles, and planets with a true mass measurement from astrometry are squares, while triangles are minimum masses (RV only). Around M dwarfs, TOI-4201 b has the highest mass ratio for transiting planets, and the planet with the highest mass ratio overall is GJ 463 b (Endl et al. 2022; Sozzetti 2023).

or there must be another process heating the interior. However, a detailed investigation of this would require next-generation evolution models and is beyond the scope of this work.

5.2. Planet Formation and Migration

Core accretion is a model of planet formation by which small solid particles coagulate and gradually grow to planetary embryos through either pebble or planetesimal formation. These embryos can be massive enough to trigger runaway gas accretion and allow for planets to retain large H/He-dominated atmospheres (Pollack et al. 1996). While this is the favored model for close-in planets, the decreased solid mass available (Andrews et al. 2013; Pascucci et al. 2016) and the increased Keplerian orbital timescales (Laughlin et al. 2004) around M

dwarfs make reaching runaway accretion and forming giant planets a challenge.

Simulations conducted under both planetesimal and pebble accretion have supported the idea that these objects are difficult to form and should therefore be uncommon. Using Generation III of the Bern model, which is underpinned by planetesimal accretion, Burn et al. (2021) found that only 2%–9% of stars with masses comparable to TOI-4201 were expected to host giant planets with their simulations. As they defined giant planets as those having $M > 100 M_{\oplus}$, it is uncertain how often those giant planets could have masses comparable to TOI-4201 b. Simulations conducted under the pebble accretion model also suggest that giant planets should be rare around low-mass stars (Liu et al. 2019a; Chachan & Lee 2023).

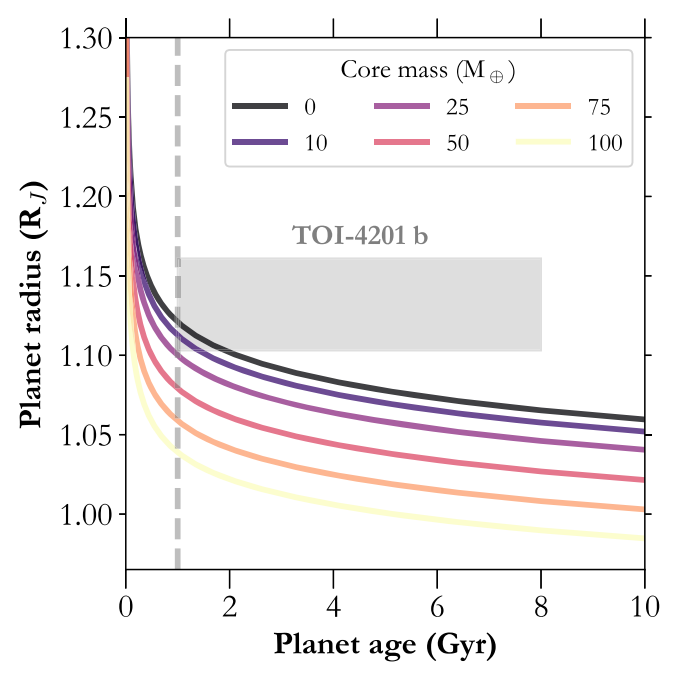


Figure 3. The radius evolution of a planet with the same mass and equilibrium temperature as TOI-4201 b assuming different core (heavy-element) masses, following the model described in Müller & Helled (2021). The gray shaded region represents $\pm 1\sigma$ for TOI-4201 b, a region substantially above the radius expected for a planet composed purely of H/He. As there are no indications that this is a particularly young system, we include a dashed line at 1 Gyr to suggest a lower limit on the age of the planet.

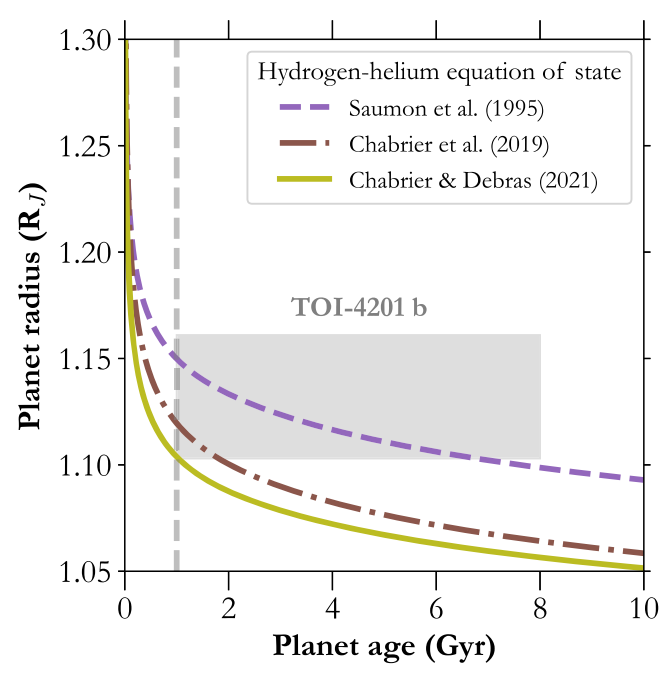


Figure 4. The radius evolution of a planet with the same mass and equilibrium temperature as TOI-4201 b assuming different H/He equations of state, following the models described in Müller et al. (2020b), Müller & Helled (2021), and S. Müller et al. (2023, in preparation). The gray shaded region represents $\pm 1\sigma$ for TOI-4201 b. As there are no indications that this is a particularly young system, we include a dashed line at 1 Gyr to suggest a lower limit on the age of the planet.

We use a basic mass budget framework to determine the possibility of TOI-4201 b forming through core accretion. TOI-4201 b seems to be inflated beyond what current theoretical

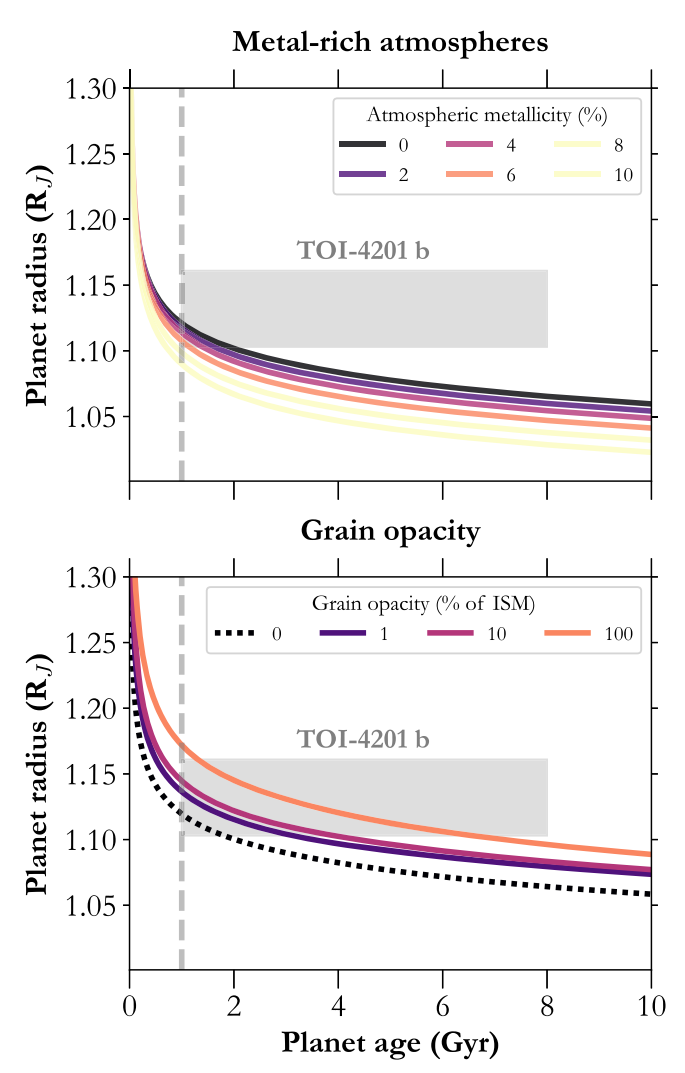


Figure 5. The radius evolution of a planet with the same mass and equilibrium temperature as TOI-4201 b assuming different (a) atmospheric metallicities and (b) grain opacities, following the models described in Müller et al. (2020b) and Müller & Helled (2021). The gray shaded region represents $\pm 1\sigma$ for TOI-4201 b. As there are no indications that this is a particularly young system, we include a dashed line at 1 Gyr to suggest a lower limit on the age of the planet.

models for giant planets support, so we are unable to meaningfully use available planetary interior and evolution models such as planetsynth to find a heavy-element content or bulk metallicity (Müller & Helled 2021). Instead, we make a lower-bound estimate of the heavy-element content by assuming the planet will have approximately the same metallicity as its host star. The composition of the Sun is approximately $1.39\% \pm 0.06\%$ metals by mass (Asplund et al. 2021). Combining this with a metallicity of 0.30 ± 0.15 dex for TOI-4201 yields an estimated heavy-element mass of $23 \pm 8 M_{\oplus}$ for TOI-4201 b. Conservatively, if we assume 10% formation efficiency (Liu et al. 2019b), this would require a minimum dust mass of $\sim 230 \pm 80~M_{\oplus}$ to have been present for planet formation in the class II disk. In the Lupus association, the dust available in class II disks around M dwarfs ranges from 1 to $50 M_{\oplus}$ (Manara et al. 2023), suggesting it is unlikely that the Atacama Large Millimeter/ submillimeter Array (ALMA) class II disk measurements indeed reflect the primordial mass budget available for the formation of TOI-4201 b through core accretion.

There are caveats to this simple argument; the efficiency of the core accretion mechanism is poorly constrained, and our understanding of the dust masses contained in disks when planet formation begins is incomplete. In our argument, we have assumed a 10% efficiency, but simulations have shown that this value is strongly dependent on both the turbulence of the disk and the fragmentation velocity of individual particles. Under reasonable disk conditions, this efficiency may range from $\sim 1\%$ up to 40% (Guillot et al. 2014; Chachan & Lee 2023). Ring structures in the protoplanetary disk may also increase formation efficiency and leave behind wide planetesimal belts with distinct profiles exterior to the planets in a system (Jiang & Ormel 2023). While a debris belt is unlikely to be detected around an older star like TOI-4201, the detection of younger GEMS may present an opportunity to look for this profile as a clue toward the formation environment of similar objects. The dust mass of a disk is typically derived by assuming blackbody emission and using single-wavelength continuum flux measurements, often in the millimeter/ submillimeter regime, combined with an assumption that the emission is optically thin (Hildebrand 1983). Recent results have shown that this is likely to underestimate the solid mass in the disks around stars of all masses; full radiative transfer modeling across multiple wavelengths has shown that continuum emission is likely optically thick (Michel et al. 2022; Xin et al. 2023), and dust masses derived by spectral energy distribution fitting are greater than the analytical estimate by a factor of 1.5-5, though this discrepancy is somewhat increased for stars more massive than M dwarfs (Rilinger et al. 2023). One possibility is that a significant amount of the dust mass is contained in larger bodies to which millimeter observations are not sensitive (Najita & Kenyon 2014). The exact amount contained in such bodies is unknown, but the upcoming next-generation Very Large Array (VLA) will be sensitive to centimeter-sized grains, and its higher resolution will allow us to probe disk substructure caused by low-mass planets (Selina et al. 2018, 2022).

Due to the gaps in our understanding, we cannot completely rule out core accretion as a formation mechanism for TOI-4201 b. However, if we assume that a substantial amount of the dust in a class II disk is contained in larger bodies, this could be indicative of planet formation beginning earlier in the lifetime of the disk (Tsukamoto et al. 2017). Class 0/I disks are more massive than their class II counterparts (Greaves & Rice 2011). but varying opacity assumptions can cause millimeter fluxderived dust masses to range from >100 M_{\oplus} (Tychoniec et al. 2018) to $<10~M_{\oplus}$ (Williams et al. 2019). Continuum fluxes from multiple ALMA or VLA bands allow for measurement of the dust opacity. Recent results with this technique have given a median dust mass of $158 M_{\oplus}$ for class 0 disks in the Perseus region (Tychoniec et al. 2020), which would only require a modest efficiency of \sim 15% to create TOI-4201 b. Formation beginning in the class I/O phase can also decrease the accretion timescale, forming a core large enough to trigger runaway gas accretion within 0.5 Myr (Tanaka & Tsukamoto 2019). Ongoing work with ALMA is looking for substructures in these early disks to better constrain when planet formation begins (Ohashi et al. 2023).

If the planet formation efficiency is <10%, another plausible formation mechanism for TOI-4201 b is gas-driven gravitational instability (GDGI; Boss 1997), whereby massive young protostellar objects (class 0 or 1) gravitationally fragment,

allowing for the material to directly collapse to form giant planets on very short timescales ($\sim 10^3 - 10^4 \text{ yr}$). Theoretically, simulations from Boss (2006, 2011) have demonstrated the possibility of giant planet formation around M dwarfs through GDGI at wide separations, followed by migration driven by the spiral arms. Subsequent work has shown that stellar irradiation at wide orbits (where the disk is optically thin) can inhibit gravitational collapse in disks $\lesssim \! \! 30\%$ in mass ratio (Cadman et al. 2020; Haworth et al. 2020; Mercer & Stamatellos 2020). However, recently, Boss & Kanodia (2023) ran a suite of formation models to show the feasibility of giant planet formation at closer separations (<5 au), where the disk is optically thick and hence more impervious to the effects of stellar irradiation. This enables the formation of giant planets with lower disk-to-star mass ratios of \sim 10%. Tobin et al. (2020), Tychoniec et al. (2020), and others have observationally shown the existence of massive protostellar objects that could be susceptible to gravitational fragmentation and possible progenitors of GEMS such as TOI-4201 b.

While the hope of differentiating between the two mechanisms and therefore gaining insight into formation efficiency through atmospheric spectroscopy is desirable (Hobbs et al. 2022), the complex and uncertain nature of the models makes any individual results more qualitative than quantitative (Mollière et al. 2022). Atmospheric spectroscopy of GEMS is now beginning with JWST (and ARIEL in the future) and may help shed light on lines of attack, or lack thereof, to this problem.

6. Summary

We present the discovery of TOI-4201 b, a Jovian exoplanet with an inflated radius orbiting an early M dwarf. The planet was first identified from TESS photometry, and follow-up observations consisting of ground-based photometry, RVs, and speckle imaging constrained the orbital parameters and allowed for characterization of the planet.

The TOI-4201 b mass ratio of $\sim 0.4\%$ is one of the highest known for transiting planets around M dwarfs. Assuming a 10% formation efficiency (Liu et al. 2019b) and a stellar/substellar atmospheric metallicity and the corresponding planetary heavy-element content of $\sim 20\,M_{\oplus}$ would require a disk with a dust mass of $\sim 200\,M_{\oplus}$. Better estimates of disk dust mass demonstrate that the most massive disks may reach this threshold, but most remain below the threshold. The existence of TOI-4201 b is suggestive of planet formation beginning before the class II disk phase.

Acknowledgments

We thank the anonymous referee for the valuable feedback that has improved the quality of this manuscript.

Data presented herein were obtained at the WIYN Observatory from telescope time allocated to NN-EXPLORE through the scientific partnership of the National Aeronautics and Space Administration, the National Science Foundation, and NOIRLab. This work was supported by a NASA WIYN PI Data Award, administered by the NASA Exoplanet Science Institute. These results are based on observations obtained with NEID on the WIYN 3.5 m telescope at KPNO, NSF's NOIRLab under proposal 2022B-785506 (PI: S. Kanodia), managed by the Association of Universities for Research in Astronomy (AURA) under a cooperative agreement with the

NSF. This work was performed for the Jet Propulsion Laboratory, California Institute of Technology, sponsored by the United States Government under prime contract 80NM0018D0004 between Caltech and NASA.

WIYN is a joint facility of the University of Wisconsin–Madison, Indiana University, NSF's NOIRLab, the Pennsylvania State University, Purdue University, the University of California–Irvine, and the University of Missouri. We thank the NEID Queue Observers and WIYN Observing Associates for their skillful execution of our NEID observations.

The authors are honored to be permitted to conduct astronomical research on Iolkam Du'ag (Kitt Peak), a mountain with particular significance to the Tohono O'odham. Data presented herein were obtained at the WIYN Observatory from telescope time allocated to NN-EXPLORE through the scientific partnership of NASA, the NSF, and NOIRLab.

Some of the observations in this paper made use of the NN-EXPLORE Exoplanet and Stellar Speckle Imager (NESSI). NESSI was funded by the NASA Exoplanet Exploration Program and the NASA Ames Research Center. NESSI was built at the Ames Research Center by Steve B. Howell, Nic Scott, Elliott P. Horch, and Emmett Quigley.

We acknowledge support from NSF grants AST-1909506 and AST-1907622 and the Research Corporation for precision photometric observations with diffuser-assisted photometry.

This work has made use of data from the European Space Agency (ESA) mission Gaia (https://www.cosmos.esa.int/gaia), processed by the Gaia Data Processing and Analysis Consortium (DPAC; https://www.cosmos.esa.int/web/gaia/dpac/consortium). Funding for the DPAC has been provided by national institutions, in particular the institutions participating in the Gaia Multilateral Agreement.

Some of the observations in this paper were obtained with the Samuel Oschin Telescope 48 inch and the 60 inch telescope at the Palomar Observatory as part of the ZTF project. ZTF is supported by the NSF under grant No. AST-2034437 and a collaboration including Caltech, IPAC, the Weizmann Institute for Science, the Oskar Klein Center at Stockholm University, the University of Maryland, Deutsches Elektronen-Synchrotron and Humboldt University, the TANGO Consortium of Taiwan, the University of Wisconsin at Milwaukee, Trinity College Dublin, Lawrence Livermore National Laboratories, and IN2P3, France. Operations are conducted by COO, IPAC, and UW.

This work makes use of observations (Proposal ID: KEY2020B-005) from the Sinistro imaging camera on the 1 m Dome B telescope at Cerro Tololo Inter-American Observatory, operated by the Las Cumbres Observatory global telescope network (LCOGT).

Computations for this research were performed on Pennsylvania State University's Institute for Computational and Data Sciences Advanced CyberInfrastructure (ICDS-ACI). This content is solely the responsibility of the authors and does not necessarily represent the views of the Institute for Computational and Data Sciences.

The Center for Exoplanets and Habitable Worlds is supported by the Pennsylvania State University, the Eberly College of Science, and the Pennsylvania Space Grant Consortium.

Some of the data presented in this paper were obtained from MAST at STScI. Support for MAST for non-HST data is

provided by the NASA Office of Space Science via grant NNX09AF08G and by other grants and contracts.

This work includes data collected by the TESS mission, which are publicly available from MAST (doi:10.17909/474x-t972). Funding for the TESS mission is provided by the NASA Science Mission directorate.

This research made use of (i) the NASA Exoplanet Archive, which is operated by Caltech, under contract with NASA under the Exoplanet Exploration Program; (ii) the SIMBAD database, operated at CDS, Strasbourg, France; (iii) NASA's Astrophysics Data System Bibliographic Services; and (iv) data from 2MASS, a joint project of the University of Massachusetts and IPAC at Caltech, funded by NASA and the NSF.

This research has made use of the SIMBAD database, operated at CDS, Strasbourg, France, and NASA's Astrophysics Data System Bibliographic Services.

This research has made use of the Exoplanet Follow-up Observation Program website, which is operated by the California Institute of Technology, under contract with the National Aeronautics and Space Administration under the Exoplanet Exploration Program.

C.I.C. acknowledges support by NASA Headquarters through an appointment to the NASA Postdoctoral Program at the Goddard Space Flight Center, administered by USRA through a contract with NASA.

G.S. acknowledges support provided by NASA through NASA Hubble Fellowship grant HST-HF2-51519.001-A awarded by the Space Telescope Science Institute, which is operated by the Association of Universities for Research in Astronomy, Inc., for NASA, under contract NAS5-26555.

Facilities: Gaia, WIYN (NEID), WIYN (NESSI), Magellan: Clay (PFS), TESS, Exoplanet Archive.

Software: ArviZ (Kumar et al. 2019), AstroImageJ (Collins et al. 2017), astroquery (Ginsburg et al. 2019), astropy (Robitaille et al. 2013; Astropy Collaboration et al. 2018), barycorrpy (Kanodia & Wright 2018), celerite2 (Foreman-Mackey et al. 2017; Foreman-Mackey 2018) exoplanet (Foreman-Mackey et al. 2021b, 2021a), ipython (Pérez & Granger 2007), lightkurve (Lightkurve Collaboration et al. 2018), matplotlib (Hunter 2007), numpy (Oliphant 2006), pandas (McKinney 2010), pyastrotools (Kanodia 2023), PyMC3 (Salvatier et al. 2016), scipy (Oliphant 2007; Virtanen et al. 2020), SERVAL (Zechmeister et al. 2018), starry (Luger et al. 2019; Agol et al. 2020), Theano (The Theano Development Team et al. 2016), planetsynth (Müller & Helled 2021).

ORCID iDs

Megan Delamer https://orcid.org/0000-0003-1439-2781 Shubham Kanodia https://orcid.org/0000-0001-8401-4300 Caleb I. Cañas https://orcid.org/0000-0003-4835-0619 Simon Müller https://orcid.org/0000-0002-8278-8377 Ravit Helled https://orcid.org/0000-0001-5555-2652 Andrea S. J. Lin https://orcid.org/0000-0002-9082-6337 Jessica E. Libby-Roberts https://orcid.org/0000-0002-2990-7613

Arvind F. Gupta https://orcid.org/0000-0002-5463-9980 Suvrath Mahadevan https://orcid.org/0000-0001-9596-7983

Johanna Teske https://orcid.org/0009-0008-2801-5040 R. Paul Butler https://orcid.org/0000-0003-1305-3761 Samuel W. Yee https://orcid.org/0000-0001-7961-3907

```
Jeffrey D. Crane https://orcid.org/0000-0002-5226-787X Stephen Shectman https://orcid.org/0000-0002-8681-6136 David Osip https://orcid.org/0000-0003-0412-9664 Andrew Monson https://orcid.org/0000-0002-0048-2586 Leslie Hebb https://orcid.org/0000-0003-1263-8637 Luke C. Powers https://orcid.org/0000-0002-5300-5353 John P. Wisniewski https://orcid.org/0000-0001-9209-1808 Jaime A. Alvarado-Montes https://orcid.org/0000-0003-0353-9741 Chad F. Bender https://orcid.org/0000-0003-4384-7220
```

Chad F. Bender https://orcid.org/0000-0003-4384-7220
Jiayin Dong https://orcid.org/0000-0002-3610-6953
Te Han https://orcid.org/0000-0002-7127-7643
Joe P. Ninan https://orcid.org/0000-0001-8720-5612
Paul Robertson https://orcid.org/0000-0003-0149-9678
Arpita Roy https://orcid.org/0000-0001-8127-5775
Christian Schwab https://orcid.org/0000-0002-4046-987X
Guðmundur Stefánsson https://orcid.org/0000-0001-7409-5688

Jason T. Wright https://orcid.org/0000-0001-6160-5888

References

```
Agol, E., Luger, R., & Foreman-Mackey, D. 2020, AJ, 159, 123
Akeson, R. L., Chen, X., Ciardi, D., et al. 2013, PASP, 125, 989
Anders, F., Khalatyan, A., Queiroz, A. B. A., et al. 2022, A&A, 658, A91
Andrews, S. M., Rosenfeld, K. A., Kraus, A. L., & Wilner, D. J. 2013, ApJ,
   771, 129
Ansdell, M., Williams, J. P., van der Marel, N., et al. 2016, ApJ, 828, 46
Asplund, M., Amarsi, A. M., & Grevesse, N. 2021, A&A, 653, A141
Astropy Collaboration, Price-Whelan, A. M., Sipőcz, B. M., et al. 2018, AJ,
   156, 123
Bailer-Jones, C. A. L., Rybizki, J., Fouesneau, M., Demleitner, M., &
   Andrae, R. 2021, AJ, 161, 147
Bakos, G. A., Bayliss, D., Bento, J., et al. 2020, AJ, 159, 267
Bensby, T., Feltzing, S., & Oey, M. S. 2014, A&A, 562, A71
Birky, J., Hogg, D. W., Mann, A. W., & Burgasser, A. 2020, ApJ, 892, 31
Boss, A. P. 1997, Sci, 276, 1836
Boss, A. P. 2006, ApJL, 637, L137
Boss, A. P. 2011, ApJ, 731, 74
Boss, A. P., & Kanodia, S. 2023, ApJ, 956, 4
Bovy, J. 2015, ApJS, 216, 29
Brown, T. M., Baliber, N., Bianco, F. B., et al. 2013, PASP, 125, 1031
Burn, R., Schlecker, M., Mordasini, C., et al. 2021, A&A, 656, A72
Butler, R. P., Marcy, G. W., Williams, E., et al. 1996, PASP, 108, 500
Cadman, J., Rice, K., Hall, C., Haworth, T. J., & Biller, B. 2020, MNRAS,
   492, 5041
Chabrier, G., & Debras, F. 2021, ApJ, 917, 4
Chachan, Y., & Lee, E. J. 2023, ApJL, 952, L20
Clanton, C., & Gaudi, B. S. 2014, ApJ, 791, 91
Collins, K. A., Kielkopf, J. F., Stassun, K. G., & Hessman, F. V. 2017, AJ,
   153, 77
Crane, J. D., Shectman, S. A., Butler, R. P., Thompson, I. B., & Burley, G. S.
   2008, Proc. SPIE, 7014, 701479
Crane, J. D., Shectman, S. A., & Butler, R. P. 2006, Proc. SPIE, 6269, 626931
Crane, J. D., Shectman, S. A., Butler, R. P., et al. 2010, Proc. SPIE, 7735,
Cutri, R. M., Skrutskie, M. F., van Dyk, S., et al. 2003, The IRSA 2MASS All-
   Sky Point Source Catalog, NASA/IPAC Infrared Science Archive, http://
   irsa.ipac.caltech.edu/applications/Gator/
Cuzzi, J. N., Estrada, P. R., & Davis, S. S. 2014, ApJS, 210, 21
Debras, F., Chabrier, G., & Stevenson, D. J. 2021, ApJL, 913, L21
Demory, B.-O., & Seager, S. 2011, ApJS, 197, 12
Duque-Arribas, C., Montes, D., Tabernero, H. M., et al. 2023, ApJ, 944, 106
Eastman, J. D., Rodriguez, J. E., Agol, E., et al. 2019, arXiv:1907.09480
Endl, M., Robertson, P., Cochran, W. D., et al. 2022, AJ, 164, 238
Feinstein, A. D., Montet, B. T., Foreman-Mackey, D., et al. 2019, PASP, 131,
   094502
Foreman-Mackey, D. 2018, RNAAS, 2, 31
Foreman-Mackey, D., Agol, E., Ambikasaran, S., & Angus, R. 2017, AJ,
Foreman-Mackey, D., Luger, R., Agol, E., et al. 2021a, JOSS, 6, 3285
```

```
Foreman-Mackey, D., Savel, A., Luger, R., et al. 2021b, exoplanet-dev/
  exoplanet v0.4.4, Zenodo, doi:10.5281/zenodo.1998447
Fulton, B. J., Rosenthal, L. J., Hirsch, L. A., et al. 2021, ApJS, 255, 14
Gagné, J., Mamajek, E. E., Malo, L., et al. 2018, ApJ, 856, 23
Gaia Collaboration, Arenou, F., Babusiaux, C., et al. 2023, A&A, 674, A34
Gan, T., Lin, Z., Wang, S. X., et al. 2022, MNRAS, 511, 83
Ginsburg, A., Sipőcz, B. M., Brasseur, C. E., et al. 2019, AJ, 157, 98
Gould, A., Dong, S., Gaudi, B. S., et al. 2010, ApJ, 720, 1073
Greaves, J. S., & Rice, W. K. M. 2011, MNRAS, 412, L88
Guillot, T., Ida, S., & Ormel, C. W. 2014, A&A, 572, A72
Halverson, S., Terrien, R., Mahadevan, S., et al. 2016, Proc. SPIE, 9908,
  99086P
Hartman, J. D., Bayliss, D., Brahm, R., et al. 2015, AJ, 149, 166
Hatzes, A. P. 2019, The Doppler Method for the Detection of Exoplanets,
  2514-3433 (Bristol: IOP Publishing), 6
Haworth, T. J., Cadman, J., Meru, F., et al. 2020, MNRAS, 494, 4130
Henden, A. A., Levine, S., Terrell, D., et al. 2018, AAS Meeting Abstracts,
  232, 223.06
Hildebrand, R. H. 1983, QJRAS, 24, 267
Hobbs, R., Shorttle, O., & Madhusudhan, N. 2022, MNRAS, 516, 1032
Hobson, M. J., Jordán, A., Bryant, E. M., et al. 2023, ApJL, 946, L4
Hoffman, M. D., & Gelman, A. 2014, JMLR, 15, 1593
Howard, S., & Guillot, T. 2023, A&A, 672, L1
Howell, S. B., Everett, M. E., Sherry, W., Horch, E., & Ciardi, D. R. 2011, AJ,
  142, 19
Huang, C. X., Vanderburg, A., Pál, A., et al. 2020, RNAAS, 4, 204
Huehnerhoff, J., Ketzeback, W., Bradley, A., et al. 2016, Proc. SPIE, 9908,
  99085H
Hunter, J. D. 2007, CSE, 9, 90
Ida, S., & Lin, D. N. C. 2005, ApJ, 626, 1045
Jiang, H., & Ormel, C. W. 2023, MNRAS, 518, 3877
Johnson, J. A., Aller, K. M., Howard, A. W., & Crepp, J. R. 2010, PASP,
Jordán, A., Hartman, J. D., Bayliss, D., et al. 2022, AJ, 163, 125
Kagetani, T., Narita, N., Kimura, T., et al. 2023, PASJ, 75, 713
Kanodia, S. 2023, shbhuk/pyastrotools, v0.3, Zenodo, doi:10.5281/zenodo.
  7685628
Kanodia, S., Mahadevan, S., Libby-Roberts, J., et al. 2023, AJ, 165, 120
Kanodia, S., & Wright, J. 2018, RNAAS, 2, 4
Kumar, R., Carroll, C., Hartikainen, A., & Martin, O. A. 2019, JOSS, 4,
Kunimoto, M., Daylan, T., Guerrero, N., et al. 2022, ApJS, 259, 33
Kurokawa, H., & Inutsuka, S.-i 2015, ApJ, 815, 78
Laughlin, G., Bodenheimer, P., & Adams, F. C. 2004, ApJL, 612, L73
Lightkurve Collaboration, Cardoso, J. V. d. M., Hedges, C., et al., 2018,
  Lightkurve: Kepler and TESS time series analysis in Python, Astrophysics
  Source Code Library, ascl:1812.013
Liu, B., Lambrechts, M., Johansen, A., & Liu, F. 2019a, A&A, 632, A7
Liu, B., Ormel, C. W., & Johansen, A. 2019b, A&A, 624, A114
Luger, R., Agol, E., Foreman-Mackey, D., et al. 2019, AJ, 157, 64
Manara, C. F., Ansdell, M., Rosotti, G. P., et al. 2023, in ASP Conf. Ser. 534,
  Protostars and Planets VII, ed. S. Inutsuka (San Francisco, CA: ASP), 539
Mandel, K., & Agol, E. 2002, ApJL, 580, L171
Mankovich, C. R., & Fuller, J. 2021, NatAs, 5, 1103
Mann, A. W., Dupuy, T., Kraus, A. L., et al. 2019, ApJ, 871, 63
Mann, A. W., Feiden, G. A., Gaidos, E., Boyajian, T., & von Braun, K. 2015,
Mann, A. W., Gaidos, E., & Aldering, G. 2011, PASP, 123, 1273
Marley, M. S., Ackerman, A. S., Cuzzi, J. N., & Kitzmann, D. 2013, in
  Comparative Climatology of Terrestrial Planets, ed. S. J. Mackwell et al.
  (Tucson, AZ: Univ. of Arizona Press), 367
McCully, C., Volgenau, N. H., Harbeck, D.-R., et al. 2018, Proc. SPIE, 10707,
   107070K
McKinney, W. 2018, in Proc. of the 9th Python in Science Conf., 445, ed.
  S. V. D. Walt & J. Millman (Austin, TX: SciPy), 56
Mercer, A., & Stamatellos, D. 2020, A&A, 633, A116
Michel, A., Sadavoy, S. I., Sheehan, P. D., Looney, L. W., & Cox, E. G. 2022,
    ApJ, 937, 104
Mollière, P., Molyarova, T., Bitsch, B., et al. 2022, ApJ, 934, 74
Monson, A. J., Beaton, R. L., Scowcroft, V., et al. 2017, AJ, 153, 96
Montes, D., González-Peinado, R., Tabernero, H. M., et al. 2018, MNRAS,
  479, 1332
Mordasini, C., Alibert, Y., Benz, W., Klahr, H., & Henning, T. 2012, A&A,
  541, A97
Mordasini, C., Klahr, H., Alibert, Y., Miller, N., & Henning, T. 2014, A&A,
```

566, A141

```
Movshovitz, N., Bodenheimer, P., Podolak, M., & Lissauer, J. J. 2010, Icar,
Movshovitz, N., & Podolak, M. 2008, Icar, 194, 368
Müller, S., Ben-Yami, M., & Helled, R. 2020a, ApJ, 903, 147
Müller, S., & Helled, R. 2021, MNRAS, 507, 2094
Müller, S., & Helled, R. 2023, A&A, 669, A24
Müller, S., Helled, R., & Cumming, A. 2020b, A&A, 638, A121
Najita, J. R., & Kenyon, S. J. 2014, MNRAS, 445, 3315
NASA Exoplanet Archive 2023, Planetary Systems, v2023-05-23 12:00,
  NExScI-Caltech/IPAC, doi:10.26133/NEA12
Ohashi, N., Tobin, J. J., Jørgensen, J. K., et al. 2023, ApJ, 951, 8
Oliphant, T. 2006, NumPy: A Guide to NumPy (USA: Trelgol Publishing), 8,
   http://www.numpy.org/
Oliphant, T. E. 2007, CSE, 9, 10
Pascucci, I., Testi, L., Herczeg, G. J., et al. 2016, ApJ, 831, 125
Pérez, F., & Granger, B. E. 2007, CSE, 9, 21
Podolak, M. 2003, Icar, 165, 428
Pollack, J. B., Hubickyj, O., Bodenheimer, P., et al. 1996, Icar, 124, 62
Rabus, M., Lachaume, R., Jordán, A., et al. 2019, MNRAS, 484, 2674
Ricker, G. R., Winn, J. N., Vanderspek, R., et al. 2014, JATIS, 1, 014003
Rilinger, A. M., Espaillat, C. C., Xin, Z., et al. 2023, ApJ, 944, 66
Robertson, P., Anderson, T., Stefansson, G., et al. 2019, JATIS, 5, 015003
Robitaille, T. P., Tollerud, E. J., Greenfield, P., et al. 2013, A&A, 558, A33
Salvatier, J., Wiecki, T. V., & Fonnesbeck, C. 2016, PeerJ Comput. Sci., 2, e55
Schönrich, R., Binney, J., & Dehnen, W. 2010, MNRAS, 403, 1829
```

Schwab, C., Rakich, A., Gong, Q., et al. 2016, Proc. SPIE, 9908, 99087H

```
Schweitzer, A., Passegger, V. M., Cifuentes, C., et al. 2019, A&A, 625, A68
Scott, N. J., Howell, S. B., Horch, E. P., & Everett, M. E. 2018, PASP, 130,
  054502
Selina, R., Murphy, E., & Beasley, A. 2022, Proc. SPIE, 12182, 1218200
Selina, R. J., Murphy, E. J., McKinnon, M., et al. 2018, Proc. SPIE, 10700,
Southworth, J., Hinse, T. C., Jørgensen, U. G., et al. 2009, MNRAS, 396, 1023
Sozzetti, A. 2023, Astronomy
                               & Astrophysics, 670, L17
Stassun, K. G., Oelkers, R. J., Pepper, J., et al. 2018, AJ, 156, 102
Stefansson, G., Mahadevan, S., Hebb, L., et al. 2017, ApJ, 848, 9
Stefansson, G., Mahadevan, S., Petrovich, C., et al. 2022, ApJL, 931, L15
Stevenson, D. J. 1982, AREPS, 10, 257
Tanaka, Y. A., & Tsukamoto, Y. 2019, MNRAS, 484, 1574
Tazzari, M., Testi, L., Natta, A., et al. 2021, MNRAS, 506, 5117
The Theano Development Team, Al-Rfou, R., Alain, G., et al. 2016,
  arXiv:1605.02688
Tobin, J. J., Sheehan, P. D., Megeath, S. T., et al. 2020, ApJ, 890, 130
Tsukamoto, Y., Okuzumi, S., & Kataoka, A. 2017, ApJ, 838, 151
Tychoniec, L., Manara, C. F., Rosotti, G. P., et al. 2020, A&A, 640, A19
Tychoniec, L., Tobin, J. J., Karska, A., et al. 2018, ApJS, 238, 19
Virtanen, P., Gommers, R., Oliphant, T. E., et al. 2020, NatMe, 17, 261
Williams, J. P., Cieza, L., Hales, A., et al. 2019, ApJL, 875, L9
Wright, E. L., Eisenhardt, P. R. M., Mainzer, A. K., et al. 2010, AJ, 140, 1868
Xin, Z., Espaillat, C. C., Rilinger, A. M., Ribas, A., & Macias, E. 2023, ApJ,
Zechmeister, M., Reiners, A., Amado, P. J., et al. 2018, A&A, 609, A12
```